Quadrature Rotating-Frame Gradient Fields For Ultra-Low Field Nuclear Magnetic Resonance and Imaging

Louis-S. Bouchard
*Materials Sciences Division, Lawrence Berkeley National Laboratory, 1 Cyclotron Rd. Bldg 11-D64, Berkeley, CA 94709**
(Dated: January 5, 2006)

Magnetic resonance imaging (MRI) in very low fields is fundamentally limited by untruncated concomitant gradients which cause severe distortions in image acquisition and volume selection if the gradient fields are strong compared to the static field. In this paper, it is shown that gradient fields oscillating in quadrature can be used for spatial encoding in low fields and provide substantial improvements over conventional encoding methods using static gradients. In particular, cases where the gradient field is comparable to or higher than the external field, $G_{max}/B_0 > 1$, are examined. It is shown that undistorted slice selection and image encoding is possible because of smaller geometric phase errors introduced during cyclic motions of the Hamiltonian. In the low field limit ($G_{max}/B_0 \rightarrow \infty$) slice selection is achieved with a combination of soft pulse segments and a coherent train of hard pulses to average out concomitant fields over the fast scale of the rf Hamiltonian.

PACS numbers: 03.50.De,07.55.Db,76.60.Pc

I. INTRODUCTION

Magnetic resonance imaging (MRI) tomography [1, 2] relies on Fourier encoding, a method by which the phase of the transverse magnetization is modulated by application of a gradient along some direction. Multiple encodings are collected, and inverse Fourier transformation of the data set provides a reconstructed map of the spin density. At high fields, this description is accurate because the spin Hamiltonian is truncated by the strong Zeeman interaction. Truncation corresponds to the averaging of rapidly oscillating concomitant components in I_X and I_Y of the gradient field perpendicular to the Zeeman field (I_Z).

At low fields, the truncated Hamiltonian no longer provides an accurate description of the spin dynamics. As the ratio G_{max}/B_0 is increased, the concomitant fields cause severe distortions in the phase encoding and slice selection. (G_{max} is the maximum gradient field over the measurement region or field of view.) When $G_{max}/B_0 \sim 1$, for example, planes of isofrequency are bent into spheres whose radius equals one half the field of view [3]. Low field NMR/MRI systems are of great interest because of the possibility of lower production and operational costs and portability of the device. There are also several intrinsic advantages including reduced magnetic susceptibility artifacts, increased T_1 contrast, spatially-resolved zero field J spectroscopy, simultaneous detection of multiple nuclei.

A recent approach by Meriles *et al.* [4] uses a rapid train of dc magnetic field pulses to eliminate the overall phase accumulated due to components of the concomitant field that are perpendicular to the axis of the π pulse. The pulse train provides spatial encoding along the direction of the pulse axis. We have recently implemented the Meriles approach in μT fields (to be published) using SQUID detection. This method, however, only applies at or near zero fields and is expected to break down at higher fields ($\gtrsim mT$) where the dynamics are better described by a rotating frame.

This article demonstrates that pairs of magnetic field gradients oscillating in quadrature produce significantly improved performance for spatial encoding and slice selection in low fields. In a regime where conventional MRI approaches are either useless or at best, perform poorly, the rotating gradient method takes advantage of stationary gradient field components in the rotating frame to provide undistorted phase encoding. The remaining oscillatory components are linearly polarized rather than circularly polarized and much less effective in perturbing the intended trajectory. Slice selection is performed with a combination of hard and soft rf pulses and rotating frame gradient fields; a coherent train of hard pulses eliminates the problematic concomitant component. Finally, I show that undistorted slice selection is possible in zero fields.

II. BACKGROUND

A. RF Fields

Consider a general Hamiltonian of the form, $\mathscr{H} = \mathscr{H}_Z + \mathscr{H}_G + \mathscr{H}_{rf}$, where $\mathscr{H}_Z$ is the Zeeman interaction with the static external field $\mathbf{B} = B_0\hat{\mathbf{z}}$ (assumed uniform and unidirectional throughout), $\mathscr{H}_G$ is the interaction of spins with the applied gradient and its concomitant fields and $\mathscr{H}_{rf}$ describes the rf field. Explicitly, $\mathscr{H}_Z = -\boldsymbol{\mu}\cdot\mathbf{B} = \omega_0 I_Z$ and $\mathscr{H}_G = -\boldsymbol{\mu}\cdot(\mathbf{r}\cdot\nabla\mathbf{B})$, where $\boldsymbol{\mu} = \gamma\mathbf{I}$, $\mathbf{I} = \sum_{i=1}^{n}\mathbf{I}_i$ and $\omega_0 = -\gamma B_0$. I include γ in the gradient scaling, so the gradient units are reported in rad/s/cm.

*URL: http://waugh.cchem.berkeley.edu

With the quantization axis along Z, a transformation to the interaction representation is effected by an operation $e^{i\omega_k I_Z t}(\cdot)e^{-i\omega_k I_Z t}$, where ω_k is the rotating frame frequency. In the notation $\mathscr{H}' = e^{i\omega_k I_Z t}\mathscr{H}e^{-i\omega_k I_Z t}$ and $\sigma' = e^{i\omega_k I_Z t}\sigma e^{-i\omega_k I_Z t}$, the equation of motion for the density operator σ' in the interaction representation is $\partial\sigma'/\partial t = -i[\mathscr{H}', \sigma']$, where $\mathscr{H}' = e^{i\omega_k I_Z t}(\mathscr{H}_Z + \mathscr{H}_G + \mathscr{H}_{rf})e^{-i\omega_k I_Z t} - \omega_k I_Z$.

1. Linear and quadratic rf excitation

The non-secular components of a linearly polarized rf pulse significantly perturb the intended trajectory. In the limit $\mathbf{B} \to 0$, spin precession takes place in the quadrupole gradient field [4]. To eliminate this possibility, it is better to consider rf fields rotating at angular frequency ω_{rf}. The lab frame Hamiltonian is $\mathscr{H}_{rf} = \omega_1 [\cos(\omega_{rf}t + \phi(t))I_X + \sin(\omega_{rf}t + \phi(t))I_Y]$ transforms to the rotating frame $\omega_k = \omega_{rf}$ as,

$$\mathscr{H}'_{rf} = 2\omega_1(t) \left[I_X \cos\phi(t) + I_Y \sin\phi(t)\right]. \tag{1}$$

where $\omega_1(t)$ is the amplitude modulation of the rf field at carrier frequency ω_{rf}, and $\phi(t)$, its phase modulation[18]. The rotating frame is usually taken to be the rf carrier frequency ($\omega_k = \omega_{rf}$), which in turn is normally tuned at the resonance frequency of the nuclear spins.

This is to be compared with the linearly polarized field $\mathscr{H}_{rf} = \omega_1(t)\cos(\omega_{rf}t + \phi(t))I_X$, whose rotating frame Hamiltonian is

$$\mathscr{H}'_{rf} = \frac{\omega_1}{2}\left[I_+(e^{2i\omega_{rf}t}e^{i\phi} + e^{-i\phi}) + I_-(e^{-2i\omega_{rf}t}e^{-i\phi} + e^{i\phi})\right]. \tag{2}$$

The rapidly oscillating terms $e^{\pm 2i\omega_{rf}t}$ are discarded at high fields (large ω_{rf}), producing an effective Hamiltonian $\mathscr{H}'_{rf} = \omega_1 [I_X \cos\phi(t) + I_Y \sin\phi(t)]$. At low fields, truncation is not justified so we use rotating rf fields in our simulations.

B. Encoding By Quadrature RF Gradients

Pairs of gradients driven by currents 90° out of phase with each other generate a field which rotates at the frequency of the rotating frame and can be used to generate stationary components for use in Fourier encoding. We discuss two different configurations.

1. Rotating Frame Gradient of the First Kind (Type I)

A gradient of the form $\mathbf{B}^{(1)}(\mathbf{r}) = a(z\hat{\mathbf{x}} + x\hat{\mathbf{z}})$, combined with another gradient field rotated by 90° about the Z axis, with respect to the first one, $\mathbf{B}^{(2)}(\mathbf{r}) = b(z\hat{\mathbf{y}} + y\hat{\mathbf{z}})$, produces a total field $\mathbf{B}(\mathbf{r}) = (\mathbf{B}^{(1)} + \mathbf{B}^{(2)})(\mathbf{r})$. The second field is driven by a current that is 90° out of phase with respect to the first field, i.e. $a(t) = g\cos(\omega_g t + \varphi)$ and $b(t) = g\sin(\omega_g t + \varphi)$. The respective Hamiltonians are,

$$\begin{aligned}\mathscr{H}_G^{(1)}(\mathbf{r}) =& zg\cos(\omega_g t + \varphi)I_X + xg\cos(\omega_g t + \varphi)I_Z,\\ \mathscr{H}_G^{(2)}(\mathbf{r}) =& zg\sin(\omega_g t + \varphi)I_Y + yg\sin(\omega_g t + \varphi)I_Z.\end{aligned}$$

The total Hamiltonian in the rotating frame is,

$$\begin{aligned}\mathscr{H}_G^{(I)\prime}(\mathbf{r}) =& zg\cos\varphi I_X + zg\sin\varphi I_Y\\ &+ g\left[x\cos(\omega_g t + \varphi) + y\sin(\omega_g t + \varphi)\right] I_Z.\end{aligned} \tag{3}$$

Taking $\varphi = 0°$ gives a time-independent Z gradient field in I_X, while $\varphi = 90°$ gives a time-independent Z gradient field in I_Y. The time-dependence of the gradient has been relinquished to an oscillating field along I_Z. It turns out that this type of Hamiltonian with linearly polarized oscillating components possesses better averaging properties than one with rotating components (see Appendix C). I will show that it performs better Fourier encoding and volume selection along Z in low fields.

2. Rotating Frame Gradient of the Second Kind (Type II)

The linear superposition of a field $\mathbf{B}^{(1)}(\mathbf{r}) = a(y\hat{\mathbf{x}} + x\hat{\mathbf{y}})$ with another field $\mathbf{B}^{(2)}(\mathbf{r}) = b(-x\hat{\mathbf{x}} - y\hat{\mathbf{y}} + 2z\hat{\mathbf{z}})$, but scaled by ϵ gives a total field $\mathbf{B}(\mathbf{r}) = (ay - \epsilon bx)\hat{\mathbf{x}} + (ax - \epsilon by)\hat{\mathbf{y}} + 2\epsilon bz\hat{\mathbf{z}}$. If these two fields are operated 90° out of phase, i.e. set $a(t) = g\cos(\omega_g t + \varphi)$ and $b(t) = g\sin(\omega_g t + \varphi)$, gives a rotating frame Hamiltonian,

$$\begin{aligned}\mathscr{H}_G^{(II)\prime}(\mathbf{r}) =& \left[-\epsilon xg\sin(\omega_g t + \varphi) + yg\cos(\omega_g t + \varphi)\right]\left(\frac{I_+e^{i\omega_k t} + I_-e^{-i\omega_k t}}{2}\right)\\ &+ \left[xg\cos(\omega_g t + \varphi) - \epsilon yg\sin(\omega_g t + \varphi)\right]\left(\frac{I_+e^{i\omega_k t} - I_-e^{-i\omega_k t}}{2i}\right)\\ &+ I_Z\left[\epsilon 2zg\sin(\omega_g t + \varphi)\right]\end{aligned} \tag{4}$$

In the special case $\epsilon = 1.0$, this field has the following features. The X gradient in the rotating frame is time-independent in I_X for $\varphi = 90°$ or in I_Y for $\varphi = 0°$. The Y gradient rotates at a rate $2\omega_g$, while the Z gradient oscillates in I_Z at rate ω_g. Likewise, stationary Y gradients in the rotating frame can be obtained by taking $\mathbf{B}^{(1)}(\mathbf{r}) = a(-y\hat{\mathbf{x}} - x\hat{\mathbf{y}})$ instead of $\mathbf{B}^{(1)}(\mathbf{r}) = a(y\hat{\mathbf{x}} + x\hat{\mathbf{y}})$, or equivalently, by inverting the sign of ϵ.

III. FOURIER ENCODING

To compare the method to conventional phase encoding, we numerically calculate the magnetization evolution under time-independent gradients and quadrature rotating-frame gradients. Rotations induced by rotating frame gradients take place about the I_Y axis. Therefore, the magnetization is nutated primarily in the XZ plane. For conventional MRI gradients, magnetization is modulated about I_Z, so that nutations would be expected to take place in the XY plane. Deviations to this expected behavior are due to non-secular gradient components.

Calculations were performed on a Pentium IV machine using FORTRAN 90 code compiled using version 8.1 of the Intel Fortran compiler for Linux. The density operator is propagated from initial to final states, using at least 100 subdivisions of the time axis per oscillation period of the rotating frame to calculate the time-ordered product of matrix exponentials [5] $U(T_c) = \prod_{i=1}^{100} \exp(-iH_i dt)$ to approximate the propagator, where H_i is a step-function approximation to $\mathscr{H}'(t)$.

A. Conventional imaging gradients

Figure 1 illustrates the effects of concomitant gradient fields on Fourier encoding for a Maxwell coil with field $\mathbf{B}(\mathbf{r}) = g(x\hat{\mathbf{x}} + y\hat{\mathbf{y}} - 2z\hat{\mathbf{z}})$ and $G_{max}/B_0 \sim 1.0$. The intent is to produce a modulation along Z. Instead of a linear phase dependence along Z, the modulation depends on X because of deviations caused by the non-secular concomitant fields. Here, $G_{max} = g \cdot FOV/2$, where $FOV = 20$ cm is the field of view. The distortions in the spatial encoding also depend on y, as can be seen by comparing Figure 1(A) to (B) and (C), which are plots of the magnetization following a constant gradient pulse applied for 40 μs. The corresponding results for the magnetization plots in YZ planes identical to the XZ planes due to the symmetry of this gradient. This renders the conventional gradient useless when the ratio G_{max}/B_0 is large.

Figure 2 shows similar plots of magnetization following a constant gradient pulse ($G_{max}/B_0 \sim 1.0$), for a Golay pair as used in conventional MRI. Such coils are normally used to provide modulations along X and Y. The total field is $\mathbf{B}(\mathbf{r}) = g(z\hat{\mathbf{x}} + x\hat{\mathbf{z}})$ and includes a concomitant component along Z. This component is responsible for the heavy distortions in the modulation profile. Figure 2(A) shows greatest distortions in the XZ ($y = 0$ cm)

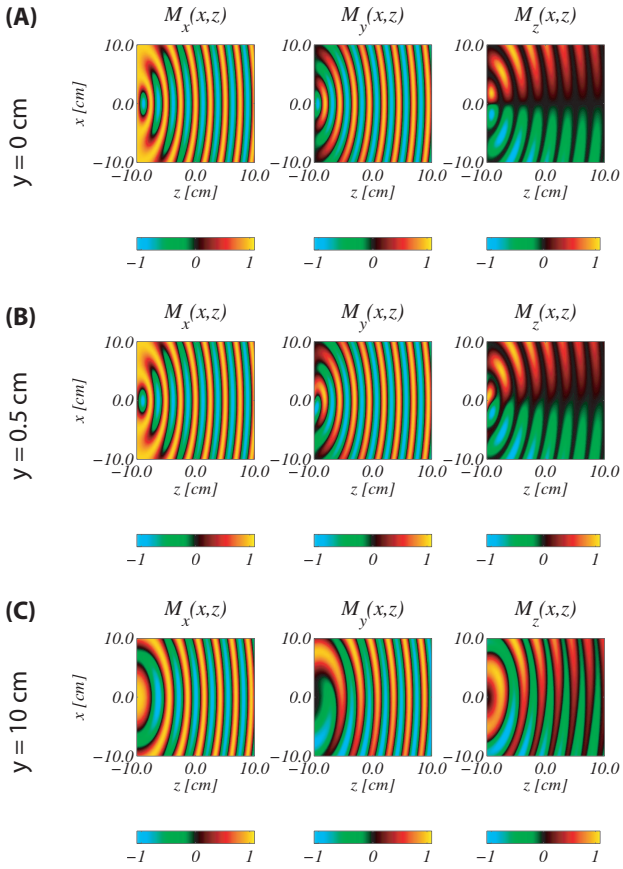

FIG. 1: (Color online) Conventional Fourier encoding along Z with Maxwell coil in the presence of concomitant gradients operated at constant current and $G_{max}/B_0 \sim 1.0$. Curved surfaces rather than planes of constant phase are produced. Magnetization along XZ for planes at (A) $y = 0$ cm, (B) $y = 0.5$ cm and (C) $y = 10$ cm.

plane. The least distortion is seen in the plot of magnetization along XY, as shown in Fig. 2(C), for the plane $z = 0$ cm. However, distortions increase with z; as seen in Fig. 2(B) for the case $z = 10$ cm.

In both cases of Maxwell or Golay pair coils, a similar behavior is observed in which curved surfaces converging towards a common attractor whose location, according to Yablonski [3], is a focal point for these concentric surfaces and the radius of curvature is $R_c = B_0/g$.

B. Rotating frame gradients

1. *Encoding in the XZ and YZ plane*

In Fig.3 are plots of the magnetization profile in a 20 cm field of view following 40 μs of evolution in a quadrature rotating-frame gradient for which $G_{max}/B_0 \sim 1.0$ ($g = 62,872$ rad/s/cm, $B_0 = 628,716$ rad/s). Figure 3(A) shows a Z modulation produced using a Type I rotating frame gradient which is to be compared with

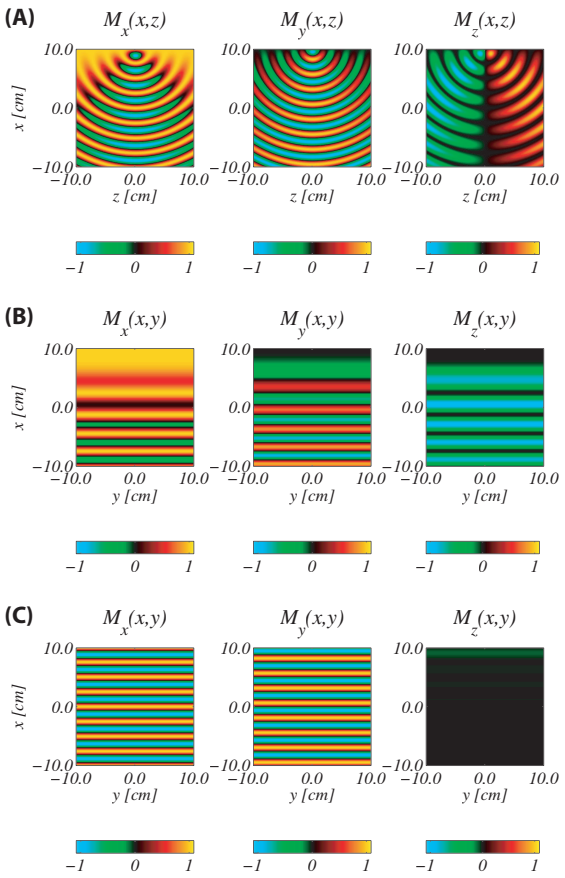

FIG. 2: (Color online) Conventional Fourier encoding along X with a saddle coil operated with constant current such that $G_{max}/B_0 \sim 1.0$ ($g = 2.35$ G/cm for 40 μs). Magnetization is plotted (A) in the XZ plane at $y = 0$ cm, in the XY plane at $z = 10$ cm (B) and at $z = 0$ cm (C).

the pattern of Fig. 1(A). The single focal point is split in two opposite attractor points, resulting in lower overall curvature of the phase profile. The smaller phase errors are due to the smaller solid angle traced by the Hamiltonian trajectory; see the discussion on geometric phase in Appendix C.

If a square region is cut out of this magnetization profile at 45° to the field of view (Fig. 3), the modulation is close to ideal, with displacements of the isofrequency sets along the direction of curvature less than 5% of the length of the corresponding isofrequency segment. The area of this reduced field of view is $1/\sqrt{2}$ the original field of view; this is equivalent to undistorted Fourier encoding with $G_{max}/B_0 \sim 0.7$.

To realize Fourier encoding of MRI slices in the XZ and YZ plane, this type of gradient presents a substantial improvement for imaging under conditions of strong gradients, i.e. when $G_{max}/B_0 \gtrsim 0.5$, over conventional static gradients. A simulated MRI image is shown in the next section which documents the improved spatial encoding.

Rotating frame Type II gradients also provide im-

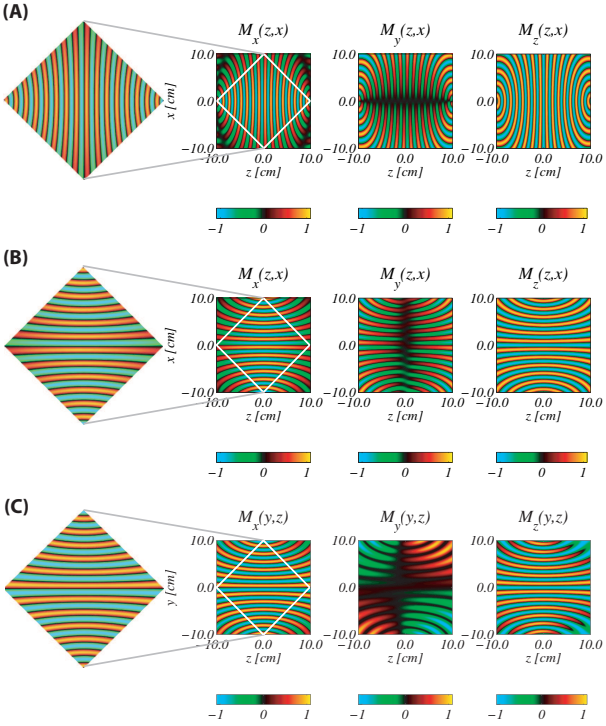

FIG. 3: (Color online) Magnetization profile following 40 μs of evolution ($G_{max}/B_0 \sim 1.0$) under (A) Type I and (B,C) Type II rotating frame gradients (with ϵ=0.5). In (B) X and (C) Y modulations are shown. Subsets of the field of view where the modulation in M_x is most uniform are enlarged.

proved spatial encoding in the case of magnetization modulations along X and Y within an XZ or YZ slice, respectively. The results in Figs. 3(B,C) were produced with a scaling factor $\epsilon = 0.5$. This choice of ϵ reduces the impact of the oscillating concomitant component along I_Z, which is responsible for much of the distortion in the encoding. This comes at the price of a slight oscillatory perturbation in the static concomitant component of the gradient along I_Y; however, results show that this error is tolerable. Again, this improved performance can be understood in terms of geometric phase (see Appendix C), with the exception of a rotating $2\omega_g$ term in the transverse plane. However, this component is small in the neighborhood of $y = 0$. The performance of this gradient degrades at large $|y|$, as shown in the next section.

As for the case of a conventional static gradient, the magnetization profile degrades further as the plane is moved away from the origin (data not shown). However, for the purposes of Fourier encoding a slice whose thickness is 1 cm, the profile is sufficiently constant across the slice thickness when $G_{max}/B_0 \sim 1.0$.

2. *Encoding in the XY plane*

Figure 4 shows that undistorted Fourier encoding along X or Y in an XY slice at $z = 0$ cm is possible only in a

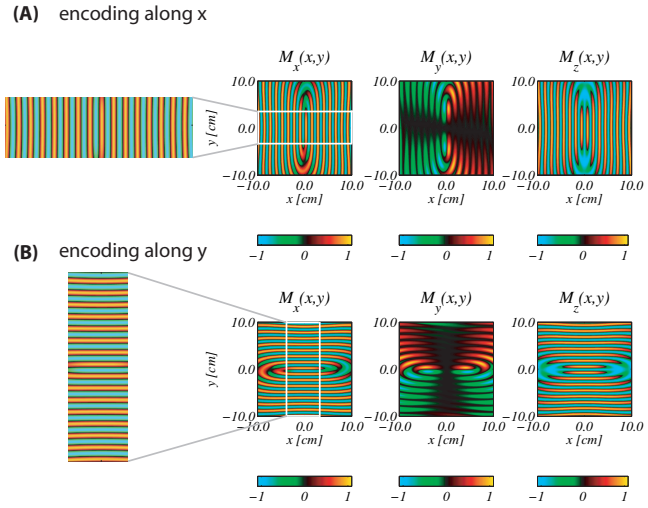

FIG. 4: (Color online) Fourier encoding along X (A) and Y (B) in the XY plane at $z = 0$ cm using Type II rotating frame gradients ($G_{max}/B_0 \sim 1.0$). Rectangular subsets of the field of view where the modulation in M_x is most uniform are enlarged.

reduced field of view, which is half the full field of view, as shown in Figs. 4(A) and (B). Encoding along X or Y in the XY plane is an instance where conventional MRI static gradients perform better than rotating frame gradients at low fields (see Fig.2C). In both cases of static gradient and rotating frame gradient fields, the performance degrades at large $|z|$ (see Fig. 2B).

C. MRI image acquisition

Distortions in the phase encoding ultimately translate into image distortions. In the limit $\mathbf{k} \to 0$, there are no significant distortions to the phase encoding simply because there is no evolution under the gradient fields. Distortions from concomitant gradients increase with spatial frequency. To illustrate image distortion effects, the phase encoding process is simulated in Fig. 5, including evolution under all non-secular field components of the Hamiltonian.

A 128×128 single show echo-planar (EPI) readout is applied to the 128×128 proton density maps of Figs. 5(A,C). Conventional high-field MRI images (Figs. 5 B,D) faithfully represent the respective proton density maps while acquisition in low field (Figs. 5 E,G) suffers from heavy distortions, ghosting and blurring over most of the field of view. ($G_{max}/B_0 \sim 3.2$ at 10 cm from the center). Most of these artifacts are absent over the middle $1/\sqrt{2}$ region of the field of view in the case of quadrature rotating-frame gradient encoding (Figs. 5 F,H).

IV. VOLUME SELECTIVITY

1. *Slice Selection with rotating frame gradients*

In previous sections, rotations about I_Y in the XZ plane were used to impart the desired spatial encoding. This means that any magnetization which is along I_Y remains along I_Y. Assuming an rf field polarized along I_X, this suggest two simple schemes for selective excitation. The first scheme uses a Type I rotating frame gradient whose Hamiltonian, $\mathscr{H}_G^{(I)\prime}$ (Eq. 3), can be made to provide a Z gradient along I_Y. The second scheme uses a Type II gradient (Eq. 4) to produce a stationary X or Y gradient along I_Y in the rotating frame.

Then, consider the following sequence of events:

1. A non-selective (hard) 90° pulse rotates the equilibrium z magnetization towards I_Y: $I_Z \to I_Y$.

2. A soft 90° pulse along I_X in the rotating frame is applied in the presence of an $I_Y\,[zg]$ (z gradient) term in the Hamiltonian.

The soft pulse will rotate I_Y towards $-I_Z$ within its bandwidth, and leave spins unaffected (i.e. pointed along I_Y) outside its bandwidth. The spins outside the pulse bandwidth will remain along I_Y since the rotating frame gradients induce nutations mostly about I_Y. With the excited spins along I_Z, spatial encoding is then performed with a rotating frame gradient. The MRI signal is contained in the X and Z components of the magnetization. A readout of M_x provides the in-phase NMR signal while permitting further subsequent encoding of this magnetization. If desired, the XZ plane can be rotated into the XY plane for a full readout of the complex magnetization.

There are two regimes of interest when considering such a selective excitation: when the rotating frame frequency is rapid compared to variations in the rf pulse envelope, and when the rotating frame is slow, as in the limit of ultra-low fields. In the first case, the rf pulse is perceived as being a constant field with a time interval dt, during which, the I_Z term oscillates back and forth possibly many times. The oscillating I_Z term will then experience a certain amount of self-averaging in the limit where the I_Z term is small. In the second limit, the field from the I_Z term appears stationary on the timescale of rf field envelope fluctuations. In this case, multipulse techniques can be used to eliminate the I_Z term during the soft pulse passage. The result is justified by Average Hamiltonian Theory (AHT) (see Appendix A). In Appendix B we describe a coherent averaging approach for eliminating the I_Z term.

A. Composite selective pulses

To minimise the phase errors that normally accrue in the presence of a gradient beyond the energy isocenter of

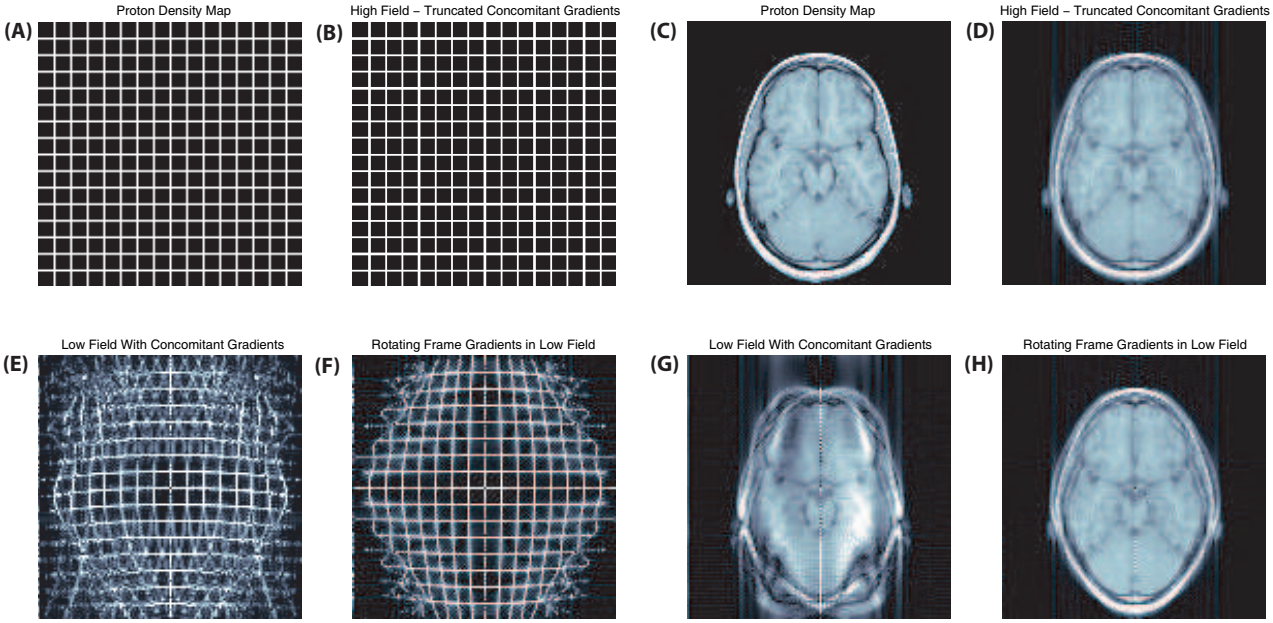

FIG. 5: Single shot EPI using proton density maps (128×128) as input parameters (A,C) for a Cartesian grid phantom (A,B,E,F) and axial slice of human brain (C,D,G,H). The 20 cm field of view (YZ plane) is phase encoded in 128×128 steps by simulating an echo-planar readout. (B,D) high field images with conventional MRI encoding gradients ($G_{max}/B_0 < 0.1$). (E,G) conventional low field MRI images ($G_{max}/B_0 \sim 3.2$) with saddle pair and Maxwell coils. (F,H) low field images ($G_{max}/B_0 \sim 3.2$) with quadrature rotating frame gradients.

TABLE I: Fourier coefficients used to construct the Geen & Freeman self-refocusing pulse (from Reference [6]).

n	A_n	B_n
0	0.23	0.00
1	0.89	-0.40
2	-1.02	-1.42
3	-0.25	0.74
4	0.14	0.06
5	0.03	0.03
6	0.04	-0.04
7	-0.03	-0.02
8	0.00	0.01

a selective pulse, it is preferrable to use a self-refocusing pulse, such as that of Geen & Freeman [6]. The envelope of the rf Hamiltonian ($0 \le t \le T_p$) in the interaction representation is a sum of Fourier components according to

$$\mathscr{H}'_{rf}(t) = \left\{ \sum_{n=0}^{8} \left[A_n \cos\left(n\frac{2\pi}{T_p}t\right) + B_n \sin\left(n\frac{2\pi}{T_p}t\right) \right] \right\} \omega_1 I_X,$$

with the coefficients (A_n, B_n) listed in Table I. The pulse envelope is shown in Fig.6(A). To get a 90° flip angle on the proton resonance with this pulse, $\omega_1 = \gamma B_1$ of approximately 600 rad/s is required. (Referring to the scaling in Fig.6(A), this corresponds to a peak rf amplitude of $\sim 2,040$ rad/s.)

To produce a selective pulse which averages out the I_Z term to zero during its course, we modify the soft pulse by inserting the following coherent train of hard pulses (see Appendix B),

$$\left\{ 2\tau - (\pi_y) - \tau - (\pi_z) - 2\tau - (\pi_{-z}) - \tau - (\pi_{-y}) - 2\tau \right\}_n . \quad (5)$$

This subunit is repeated n times, for the entire duration of the soft pulse and its duration should be short compared to the time scale of fluctuations in the soft pulse envelope. We show later that for a Geen & Freeman pulse, τ should be roughly three orders of magnitude less than the pulse duration; the exact figure ultimately depends on the shape of the soft pulse with smoother shapes generally less demanding of the coherent train. The new pulse will be slightly longer; its length increases by the total duration of the hard pulses added. The new pulse is sketched in Fig. 6(B). This procedure introduces two widely different time scales to the pulse whose fine structure naturally averages out, as explained in Appendix A.

B. Slice selection in ultra-low fields

We first examine the case of weak gradients ($G_{max}/B_0 \sim 0.16$). The slice profile of the Geen & Freeman pulse for a slice selection along X is shown

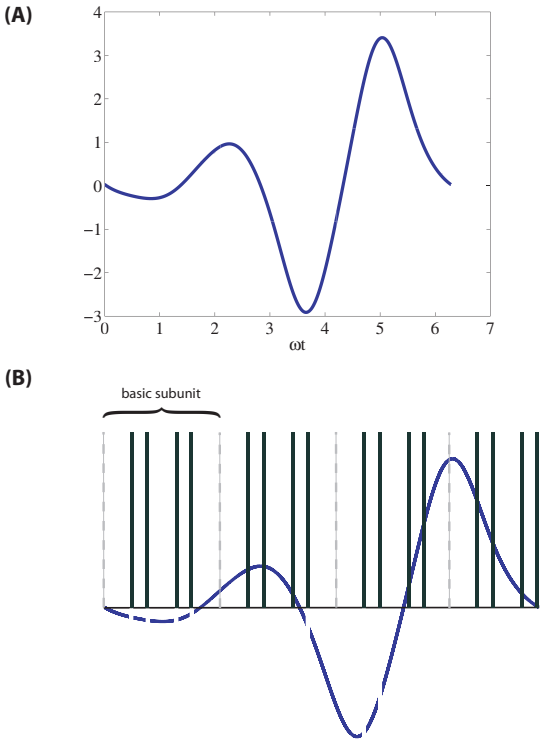

FIG. 6: (A) Amplitude modulation for the Geen & Freeman self-refocusing pulse. (B) New composite selective pulse for low field imaging takes the soft pulse and inserts the coherent train of hard pulses for the entire duration of the soft pulse. The duration of the new pulse is increased by the total length of all the hard pulses. For clarity, only a few subunits are sketched.

in Fig. 7(E) under conditions of no concomitant gradients. Figure 7(F) shows the corresponding distortion in the slice selection profile, in the form of a slight curvature, when concomitant gradients from a saddle pair coil are turned on ($G_{max}/B_0 \sim 0.17$). For a Type II gradient with $\epsilon = 1.0$, undistorted slices are obtained for XZ planes at $y = 0$ cm and $y = -10$ cm, as seen in Figs. 7(A) and (B). Similarly, undistorted slice selection can be obtained along Z using Type I rotating frame gradients. This is observed in Figs. 7(C) and (D) for the case $y = -10$ cm and $y = 0$ cm, respectively. The corresponding slices for a constant Z gradient from a Maxwell coil are shown in Figs. 7(G) and (H).

The more interesting case is $G_{max}/B_0 \gtrsim 1.6$, where conventional MRI slice selection schemes are incapable of producing slices without a severe amount of distortion. Whether the excitation is on- or off-axis makes no difference, as seen in Fig. 8(A) and (D) for a slice selection along X. The slice profile is heavily distorted into a spherical shell and there is a significant amount of excitation occurring outside the intended slice. Figures 8(B) and (C) illustrate that slice selection on-axis ($y = 0$ cm) along X or Y using a Type II rotating frame gradient with $\epsilon = 1.0$. While the performance is slightly degraded when going off-axis ($|y| = 10$ cm), as seen in Figs. 8(E) and (F), the degradation is far less important than the conventional case of Fig. 8(A) and (D), and such distortions are only significant near the edges ($|y| > 8$ cm) of the volume.

The effects of concomitant gradients on slice selection were first analyzed by Gao *et al.* [7]. Yablonskiy *et al.* [3] point out a slice curvature effect when surfaces of constant frequency $\omega = \gamma\left[(B_0 + G_x x)^2 + (G_x z)^2\right]^{1/2}$ are excited by the rf pulse. In the case of an applied X gradient of strength G_x from a Golay pair, these become cylindrical surfaces $(x - x_c)^2 + z^2 = R_x^2$ of radius $R_x = |x + B_0/G_x|$ and $x_c = -B_0/G_x$ rather than a plane at $x = x_0$, where $x_0 = (\omega/\gamma - B_0)/G_x$. For applied Z gradients, the surfaces of constant frequency are ellipsoids of revolution [3]. It is generally difficult to predict analytically the effects of non-secular concomitant components in the rotating frame. These components lead to excitation of spins outside the slice region, as seen in Figs.9(A,B) and 8(A,D).

The case of conventional slice selection with an applied Z gradient from a Maxwell coil ($G_{max}/B_0 \sim 1.6$) is shown in Figs.9(A,B). The performance is slightly better than a Golay pair generating an orthogonal slice on-axis (compare Figs.9B and 8A). Unfortunately, the slice profile suffers from a heavy elliptical curvature and strong contamination originating from outside the intended volume. At any rate, it is clear that conventional MRI gradient encoding performs poor slice selection in the regime $G_{max}/B_0 \sim 1.6$. In contrast, a Type I rotating frame gradient provides clean slice selection both on- and off-axis, as seen in Figs. 9(C) and (D). This Type I gradient performs equally well in the asymptotic regime $G_{max}/B_0 \gtrsim 25$ (data not shown).

The Type I gradient performs better than a Type II gradient for slice selection because the Type I gradient only has 2 concomitant field components and it is possible to align the rf field with the third axis. On the other hand, a Type II gradient has 3 concomitant fields, one along each axis. The main distortion effects arise from contamination of the rf excitation by the third concomitant component that is parallel to it.

C. Slice selection in zero fields

Slice selection in zero field is a relatively simple matter since there are no time-dependent gradients. While it can be viewed as the limit $G_{max}/B_0 \to \infty$ of the previous selection schemes, there is an important difference in that only a single gradient field is required for the slice selection because quadrature excitation is not needed. Moreover, a 2-component gradient field should be used, rather than 3-components, because there the third component no longer self-averages due to oscillatory time dependence.

A field such as $\mathbf{B}(\mathbf{r}) = a(z\hat{\mathbf{x}} + x\hat{\mathbf{z}})$ can be used to provide slice selection along X or Z in the following manner. For a Z slice, a selective pulse field is applied along I_Y

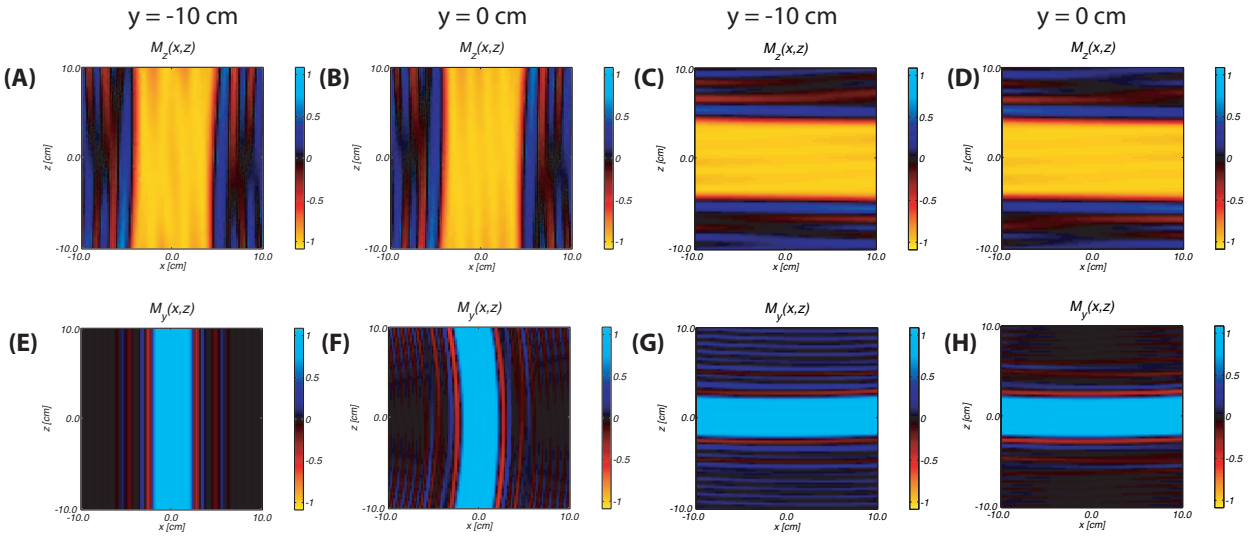

FIG. 7: (Color online) Conventional and rotating frame gradient slice profiles at $G_{max}/B_0 \sim 0.17$. (A,B) is an X slice selection (XZ plane shown) using a Type II rotating frame gradient. The undistorted slice profile (concomitant fields turned off), as would be seen in high field, is shown in (E). (F) is the corresponding profile from a conventional X gradient with concomitant fields. Comparing (B) with (F) shows that curvature is eliminated. (G,H) are conventional X slices showing a small amount of curvature. In (C,D) is the slice selection for a Type I rotating frame gradient. The effects of going off-axis are illustrated by the planes at $y = -10$ cm (plots A, C and G). Parameters were: $\epsilon = 1.0$, τ=31.5 μs, T_{sub}=252 μs (80 subunits per soft pulse), T_{puls}=10 ms, N_{sub}=39 subunits per soft pulse, $g = 856$ rad/s/cm, $\omega_g = \gamma B_0 = 50,400$ rad/s (1 cycle lasts 125 μs) and FOV = 20 cm.

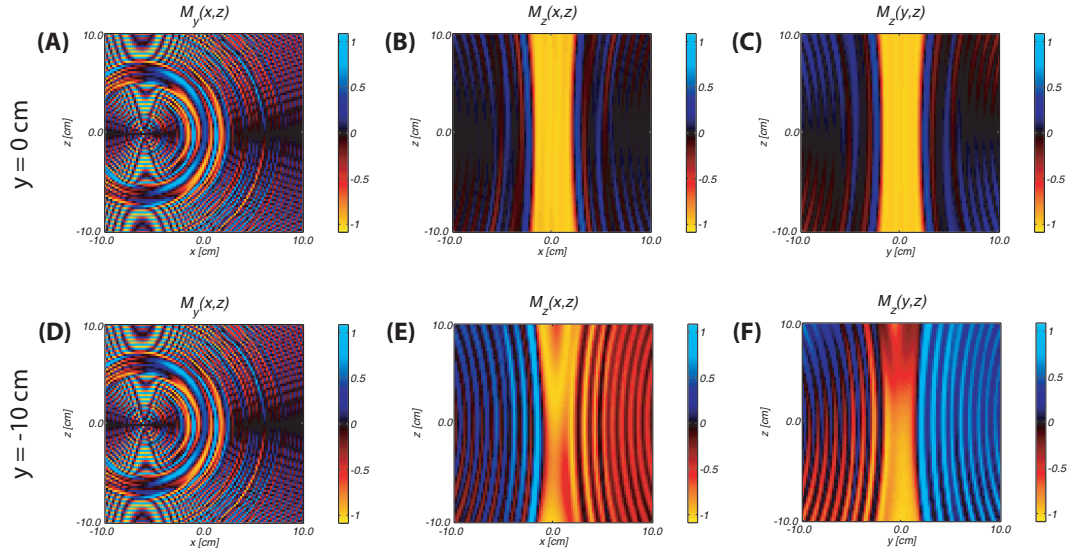

FIG. 8: (Color online) Comparison of static and Type II rotating frame gradients for slice selection in the case $G_{max}/B_0 \sim 1.6$. Plots (A,D) are the slice selection profiles for a saddle pair gradient along X for XY planes at $y = 0$ cm and $y = -10$ cm, respectively. (B,E) is the X slice selection using Type II gradients with a stationary X gradient. (C,F) is the Y slice selection for a Type II gradient with stationary Y gradient field. Parameters were: τ=15.75 μs, T_{sub}=126 μs, T_{puls}=10 ms, N_{sub}=79 subunits per soft pulse, $g = 1,605$ rad/s/cm, $\omega_g = \gamma B_0 = 10,080$ rad/s (1 cycle lasts 623μs; there are 16 cycles across the pulse duration).

and the I_Z component is eliminated using the pulse train of Eq. 5. For an X slice, a selective pulse is applied along I_X with a coherent train of hard pulses to eliminate the I_X term. Likewise, a field $\mathbf{B}(\mathbf{r}) = a(z\hat{\mathbf{y}} + y\hat{\mathbf{z}})$ can provide Y and Z slice selection. The Y slice is obtained, for example, by applying the selective pulse along I_X and eliminating the I_Y term using the coherent train of Eq. B1.

In Fig.10(A) it is clear that conventional soft pulses in zero field ($G_{max}/B_0 \rightarrow \infty$) with concomitant gradients

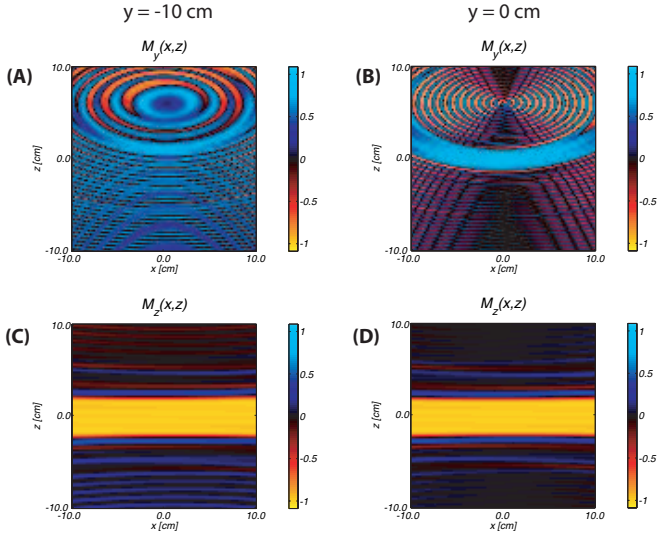

FIG. 9: (Color online) Comparison of slice selection along Z for a conventional Maxwell coil and a Type I rotating frame gradient. Plots (A,B) are for the static Maxwell coil. (C,D) is for a Type I gradient. XZ planes are aligned according to: (A,C) 10 cm off-center and (B,D) on-axis. Parameters were: τ=15.75 μs, T_{sub}=126 μs, T_{puls}=10 ms, N_{sub} = 79 subunits per soft pulse, $g = 1,605$ rad/s/cm, $\omega_g = \gamma B_0 = 10,080$ rad/s (1 cycle lasts 623μs; there are 16 cycles across the pulse duration) so that $G_{max}/B_0 \sim 1.6$ and FOV = 20 cm. Nearly identical performance is obtained at $G_{max}/B_0 \sim 25$.

are incapable of slice selection. The magnetization plots in Figs. 10(B-D) show that good slice selection can be achieved over a range of values for the inter-pulse spacing τ. At $\tau = 20$ μs and beyond, the slice profile begins to break down, as excited magnetization outside the slice of interest begins to contaminate the signal.

Thus, a soft pulse can be altered using a train of hard, composite pulses to eliminate effects of concomitant fields during the slice selection process of an MRI experiment in zero field. Results suggest that, for good performance, the inter-pulse spacing τ should be three orders of magnitude shorter than the soft pulse duration. Ultimately, this depends on the pulse shape, with flatter soft pulse shapes requiring refocusing less frequently.

V. DISCUSSION

Rotating frame gradients possess better properties for spatial encoding than conventional static gradients in the ultra-low field regime, where non-secular terms in the Hamiltonian must be included in the analysis. Since the nutations of magnetization under the gradient primarily occur about an axis in the transverse plane, the gradients act as excitation pulses and the effects of magnetic field inhomogeneities and susceptibility artifacts during gradient evolution are not of concern.

As mentioned previously, quadrature rf excitation and rotating frame gradient fields reduce the impact of non-secular terms in the Hamiltonian. These improvements are most beneficial when Fourier encoding coronal or sagittal planes (XZ or YZ), as seen in Fig.(3), or when selecting a slice in a strong gradient (Figs.8 and 9). In zero fields, slice selection is also possible along any axis using a combination of soft pulse and coherent train of hard dc pulses (Fig. 10). The EPI images of Fig. 5 demonstrate that nearly undistorted image encoding is possible in regimes where the concomitant gradient fields are several times stronger than the Zeeman field.

While the time dilation factor in the average Hamiltonian characterizing the coherent part of the selective pulse, $\mathscr{H}^{(0)\prime} = \frac{1}{2}(aI_x + cI_z)$ (see Appendix B), is equivalent to scaling down the gradient amplitudes by a factor of 2, the results of Figs.(10) and (9) show that slice selection can be done in conditions where $G_{max}/B_0 \gtrsim 25$ and $G_{max}/B_0 \to \infty$, respectively. These two regimes are well beyond the scope of applicability of conventional slice selection pulse and gradient methods. Immunity to distortions (Fig. 9) can be achieved under conditions where the gradient field is an order of magnitude larger than the static field. Applications are not limited to imaging, but include undistorted pulsed-field gradient diffusion measurements and coherence pathway selection in low fields.

Rf gradients have been successfully implemented for NMR spectroscopy and imaging by several investigators [8–10], however, their advantageous properties for low field imaging when used in quadrature appear to have been overlooked. The gradient fields discussed herein can be generated using tune and matched circuits [8]. Low cost NMR spectrometers for low field imaging can be assembled on a desktop PC using commercially-available integrated multi-channel waveform generators. Rapid point readouts interleaved with oscillating gradient pulses have been implemented by Raulet *et al.* [8]. Further speed improvements are possible with active Q-switched circuits [9] to suppress residual coil ringing. While rf power deposition from oscillating gradients and rf pulses is an important concern at high fields, this is generally not an issue at low fields, where rf absorption is orders of magnitude less.

VI. CONCLUSION

In this article, I have shown that distortions in the Fourier encoding at ultra-low magnetic fields can be substantially reduced by using quadrature rotating-frame gradients. These impart significantly less phase errors in the encoding. Rather than attempting to eliminate them, the concomitant fields are utilized to provide the required encoding. Calculations show that phase encoded and slice selective MRI is possible in ultra-low fields using a class of pulses that are combinations of soft and hard pulses to average out undesirable gradient components in zero and low fields.

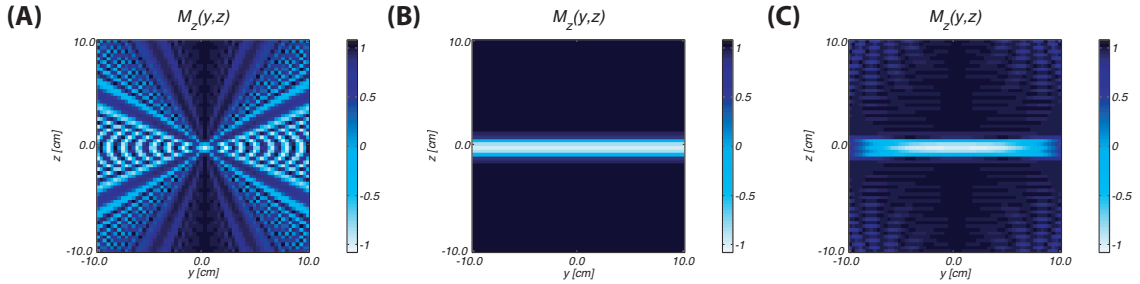

FIG. 10: Slice selection in zero field. (A) soft pulse in zero field with concomitant gradients. (B,C) soft pulse combined with train of hard pulses to eliminate the concomitant component for an interpulse spacing of (B) $\tau = 1\ \mu s$ and (C) $\tau = 20\ \mu s$. Longer τ correspond to composite pulse trains that contain less hard pulses, for a fixed soft pulse duration.

Acknowledgments

This work was supported by the Director, Office of Science, Basic Energy Sciences, U.S. Department of Energy under Contract No. DE-AC02-05CH11231. The author acknowledges useful discussions with Nathan Kelso, Vasiliki Demas, Drs. Alexander Pines, Dimitris Sakellariou, Carlos Meriles and John Clarke.

APPENDIX A: RF PULSE HAMILTONIANS WITH TWO TIME SCALES

This section contains a simple explanation of the composite slice-selective pulse in terms of the Average Hamiltonian Theory (AHT) of Waugh and Haeberlen [11–13]. On the fine scale, AHT describes the effective Hamiltonian locally while smooth fluctuations on the coarse scale provide the desirable selective properties of the pulse in low fields.

Let t be the *fast variable* and T be the *slow variable* [14, 15]. The fast scale is related to the slow scale via a small parameter ϵ, by $t = T/\epsilon$. For a function of two length scales, $\sigma(T,t) = \sigma(T, T/\epsilon)$, the chain rule for differentiation gives

$$\frac{d}{dT} = \frac{\partial}{\partial T} + \left(\frac{1}{\epsilon}\right)\frac{\partial}{\partial t}.$$

If the Hamiltonian contains slow and fast dynamics, it is an explicit function of T and t, i.e. $\mathscr{H} \equiv \mathscr{H}(T,t)$, and so will be the density operator $\sigma \equiv \sigma(T,t)$. Since ϵ is a small parameter, $\mathscr{H}(T,t)$ and $\sigma \equiv \sigma(T,t)$ can be formally expanded as one-parameter families of operators,

$$\begin{aligned}\mathscr{H}^\epsilon(T,t) =& \epsilon^l \mathscr{H}_0(T,t) + \epsilon^{l+1}\mathscr{H}_1(T,t) + O(\epsilon^{l+2}),\\ \sigma^\epsilon(T,t) =& \epsilon^l \sigma_0(T,t) + \epsilon^{l+1}\sigma_1(T,t) + O(\epsilon^{l+2}).\end{aligned}$$

The homogenization limit is $\epsilon \to 0$. The case where $\mathscr{H}^\epsilon(T,t)$ and $\sigma^\epsilon(T,t)$ are periodic in t is particularly simple. Since $\mathscr{H}$ is $O(1)$, $l = 0$, and substitution into the Liouville von Neumann equation $d\sigma/dT = -i[\mathscr{H}, \sigma]$ gives,

$$\begin{aligned}(\partial_T + (1/\epsilon)\partial_t)(\sigma_0 + \epsilon\sigma_1 + O(\epsilon^2)) =& \\ -i[\mathscr{H}_0 + \epsilon\mathscr{H}_1 + O(\epsilon^2), \sigma_0 + \epsilon\sigma_1 + O(\epsilon^2)]&.\end{aligned}$$

Identifying the powers of ϵ gives, in the lowest order,

$$\begin{aligned}\epsilon^{-1}:&\quad \partial_t\sigma_0(T,t) = 0,\\ \epsilon^{0}:&\quad \partial_T\sigma_0(T,t) + \partial_t\sigma_1(T,t) = -i[\mathscr{H}_0(T,t), \sigma_0(T,t)].\end{aligned}$$

The first equation implies that $\sigma_0 \equiv \sigma_0(T)$ is independent of the fast variable t. This is the *homogenized density operator*. Taking the time average of the second equation over one period, and using the t-periodicity of $\sigma_1(T,t)$, i.e.

$$\frac{1}{t_c}\int_0^{t_c} \partial_t\sigma_1(T,t)dt = \frac{1}{t_c}\left(\sigma_1(T,t_c) - \sigma_1(T,0)\right) = 0,$$

gives an equation of motion that is identical in form to the Liouville von Neumann equation,

$$\frac{\partial\sigma_0(T)}{\partial T} = -i[\overline{\mathscr{H}}_0(T), \sigma_0(T)],$$

where $\overline{\mathscr{H}}_0(T) = (1/t_c)\int_0^{t_c}\mathscr{H}_0(T,t)dt$ is the *homogenized Hamiltonian*, which we also recogize to be identical with the zeroth order average Hamiltonian in the Magnus expansion.

In the homogenized limit, $\lim_{\epsilon\to 0}\mathscr{H}^\epsilon(T,t) = \mathscr{H}_0(T,t)$ almost everywhere. For Hamiltonians which are everywhere bounded, i.e. $\|\mathscr{H}^\epsilon(T,t)\| \le H(T,t)$ for some $H(T,t)$ such that $\int_0^{t_c} H(T,t)dt < \infty$, Lebesgue's dominated convergence theorem gives $\lim_{\epsilon\to 0}\int_0^{t_c}\mathscr{H}^\epsilon(T,t)dt = \int_0^{t_c}\mathscr{H}_0(T,t)dt$. The boundedness requirement for the rf Hamiltonian is not a problem in practice (a physical bound is given by the maximum achievable rf field amplitude).

Thus, a soft pulse combined with a fast train of coherent hard pulses is a Hamiltonian with two time scales $(\mathscr{H}_{rf}+\mathscr{H}_G)'(t,T)$. Averaging over one period removes the dependence on t, the fast scale, giving the homogenized Hamiltonian $\overline{(\mathscr{H}_{rf}+\mathscr{H}_G)}'(T)$. Consider the following two cases.

In the zero field case ($B_0 = 0$), $\mathscr{H}_G' = gzI_X + gxI_Z$ and $\mathscr{H}_{rf}' = \omega_1(t)I_Y$. Therefore, $\overline{(\mathscr{H}_{rf}+\mathscr{H}_G)}' = \omega_1(t)I_Y + gzI_X$ for a soft pulse $\omega_1(t)$ which contains the coherent pulse train of Eq.(B2). In the low field case with a Type I gradient, $\mathscr{H}_G^{(I)\prime}$ is given by Eq.(3) with $\varphi = 0°$, so that $\overline{(\mathscr{H}_{rf}+\mathscr{H}_G)}' = zgI_X + \omega_1(t)I_Y + \overline{g[x\cos(\omega_g t) + y\sin(\omega_g t)]}I_Z$. If $2\pi/\omega_g$ is large compared to the duration of a subunit (8τ), the time-dependent term is nearly constant from the perspective of the coherent pulse train and the I_Z term vanishes. For the calculation with $G_{max}/B_0 \sim 25$ mentioned in Fig.(9) caption, $2\pi/\omega_g$ was 9740 μs and 8τ was 126 μs. The results in Fig.(9)(C,D), have $G_{max}/B_0 \sim 1.6$ ($2\pi/\omega_g = 623$ μs and $8\tau = 126$ μs) and the performance is still good. The averaging worsens for lower values of G_{max}/B_0, however, this corresponds to the high field regime where truncation in conventional MRI is efficient and the coherent train of pulses is no longer necessary or desirable.

APPENDIX B: COHERENT AVERAGING IN COMPOSITE SELECTIVE PULSES

Suppose we would like to eliminate the I_Y term of the Hamiltonian and use the I_X term for spatial encoding. Two possible approaches can be considered. The first method eliminates I_Y by a fast train of 180° pulses applied along I_X. This transforms $I_Z \rightarrow -I_Z$ and $I_Y \rightarrow -I_Y$ and the I_Y and I_Z terms of the effective Hamiltonian vanish in the limit of short inter-pulse spacings.

The second method eliminates only the I_Y term and is required in the following situation: rf or dc field along I_X, slice selective gradient field along I_Z, and concomitant gradient along I_Y. Consider the sequence of four pulses:

$$\left\{2\tau-(\pi_x)-\tau-(\pi_y)-2\tau-(\pi_{-y})-\tau-(\pi_{-x})-2\tau\right\}_n. \quad \text{(B1)}$$

The refocusing pulses are short, hard pulses, in between which the spins evolve under an arbitrary Hamiltonian of the form $\mathscr{H}'(t) = a(t)I_X + b(t)I_Y + c(t)I_Z$. Over this period of duration 8τ, this pulse sequence produces a zeroth order average Hamiltonian $\mathscr{H}^{(0)\prime} = \frac{1}{2}(\overline{a}I_X + \overline{c}I_Z)$, where $\overline{a}$ is the time average of a. In the Magnus expansion, the I_Y term is $o(\tau)$ and the scaling factor 1/2 for I_X and I_Z causes a time dilation. Similarly, the following sequence removes the I_Z term:

$$\left\{2\tau-(\pi_y)-\tau-(\pi_z)-2\tau-(\pi_{-z})-\tau-(\pi_{-y})-2\tau\right\}_n. \quad \text{(B2)}$$

motion $\mathscr{H}^A(s)$	α [rad]	B_{eff} [rad/s]	ϕ_{tot} [rad]	ϕ_{dyn} [rad]	f %	$\phi_{tot}-\phi_{dyn}$ [rad]	$\Omega(\alpha)$ [ster.]
	0.1	10.0	9.89	9.87	0.2	0.02	0
	0.1	20.0	19.75	19.75	0.0	0.0	0
	0.2	10.0	9.98	9.87	0.1	0.11	0
	0.2	20.0	19.77	19.75	0.1	0.02	0
$\mathscr{H}^C(s)$							
	0.1	10.0	10.03	9.87	1.6	0.16	0.0314
	0.1	20.0	19.78	19.77	0.1	0.01	0.0314
	0.2	10.0	10.56	9.87	7.0	0.69	0.1252
	0.2	20.0	19.86	19.75	0.6	0.11	0.1252

TABLE II: The parameter $f = 100\% \times [(\phi_{tot}-\phi_{dyn})/\phi_{dyn}]$ gives the percentage geometric phase relative to the dynamical phase. The solid angle of the motion is $\Omega(\alpha) = \int \mathrm{d}\Omega = \int_0^{2\pi}\int_1^{\cos\alpha} \mathrm{d}(\cos\theta)\mathrm{d}\phi$.

APPENDIX C: GEOMETRIC PHASE

The nutation motion of the magnetization vector when the effective field traces a closed loop results in two contributions to the phase: the dynamical phase which is proportional to the time integral of the effective field, $\phi_{dyn} = \int_0^t \gamma|B_{eff}(t')|dt'$, and a geometric phase [16, 17] which is related to the path traced by a vector in parameter space. In MRI, the motion is classical and described by a Hannay's phase. For parallel transport, the geometric phase is proportional to the solid angle subtended by the motion relative to a nearby degeneracy.

The better performance of rotating frame gradients over conventional MRI encoding gradients can be understood in terms of geometric phase. The I_Z term in a Type I Hamiltonian perturbs the path of the gradient-induced nutation in I_Y such that the solid angle subtended by the Hamiltonian path in parameter space is zero. In the case of conventional MRI, the gradient in I_Z is perturbed by oscillating components in the XY plane whose Hamiltonian traces a closed path with nonzero solid angle. The consequence of this is a bigger phase error.

The contribution from geometric phase can be calculated exactly by comparing the dynamic phase to the actual phase during one cycle of evolution. The Hamiltonian is a map $\mathscr{H} : [0, 2\pi] \rightarrow \mathfrak{h}$ which describes a curve in the vector space $\mathfrak{h}$ spanned by the operators $\{I_X, I_Y, I_Z\}$. The two distinct cases of an arclength vs. circular trajectory are to be compared. In the former case, the solid angle is zero but not in the latter case.

An arclength trajectory is defined by the curve $\mathscr{H}^A(s) = I_Y\omega_1\sin\alpha\sin s + I_Z\omega_1\sqrt{1-(\sin\alpha\sin s)^2}$, which begins parallel to I_Z, then tilts by an angle α towards $-I_Y$, then towards $+I_Y$ and back to I_Z along a geodesic path. Likewise, we define a circular trajectory by $\mathscr{H}^C(s) = I_X\omega_1\sin\alpha\cos s + I_Y\omega_1\sin\alpha\sin s + I_Z\omega_1\cos\alpha$, where α is the spherical polar angle measured from the I_Z axis. The initial density matrix I_X is propagated using $N = 80$ steps with propagators of the form $U_j^{C/A} = \exp\left[-i\mathscr{H}^{C/A}(T_j)\mathrm{d}t\right]$, $j = 1, \ldots, N$

with $\omega_1 = B_{eff}/N$ during one revolution about I_Z and $T_j = 2\pi j/N$.

During the trajectory, the geometric phase is measured as the total angle traced by the magnetization vector, including all windings, as the magnetization nutates about the Z axis while mostly remaining near the XY plane. The angles are tabulated in Table II. In support of the quadrature rotating frame gradients, we note the relative phase errors (f parameter) which are nearly an order of magnitude larger for the circular trajectory $\mathscr{H}^C(s)$ than the arclength geodesic trajectory $\mathscr{H}^A(s)$.

[1] P. Callaghan, *Principles of nuclear magnetic resonance microscopy* (Oxford : Clarendon Press, New York, 1991).
[2] P. Lauterbur, Nature **242**, 190 (1973).
[3] D. Yablonskiy, A. Sustanskii, and J. Ackerman, J. Magn. Reson. **174**, 279 (2005).
[4] C. Meriles, D. Sakellariou, A. Trabesinger, V. Demas, and A. Pines, Proc. Natl. Acad. Sci. USA **102**, 1840 (2005).
[5] N. Higham, SIAM J. Matrix Anal. Appl. **26**, 1179 (2005).
[6] H. Geen, S. Wimperis, and R. Freeman, J. Magn. Reson. **85**, 620 (1989).
[7] J. Gao, A. Anderson, and J. Gore, Phys. Med. Biol. **37**, 1705 (1992).
[8] R. Raulet, D. Grandclaude, F. Humbert, and D. Canet, J. Magn. Reson. **124**, 259 (1997).
[9] D. Cory, F. Laukien, and W. Maas, J. Magn. Reson. Series A **113**, 274 (1995).
[10] D. Hoult, J. Magn. Reson. **33**, 183 (1979).
[11] U. Haeberlen, *High resolution NMR in solids, Adv. mag. Reson.* (Academic Press, New York, 1976), suppl. 1 ed.
[12] U. Haeberlen and J. Waugh, Phys. Rev. **175**, 453 (1968).
[13] M. Mehring, *Principles of high resolution NMR in solids* (Springer-Verlag, Berlin, 1983).
[14] L. Bouchard and W. Warren, Phys Rev B **70**, 224426 (2004).
[15] S. Torquato, *Random heterogeneous materials: microstructure and macroscopic properties* (Springer, New York, 2002).
[16] M. Berry, Royal Society of London Proceedings Series A **392**, 45 (1984).
[17] *Geometric phases in physics*, Advanced Series in Mathematical Physics, Vol 5 (World Scientific, New York, 1988), A. Shapere and F. Wilczek ed.
[18] For clarity, we drop the functional dependence from the notation and write $\phi \equiv \phi(t)$, $\omega_1 \equiv \omega_1(t)$ and $\mathscr{H} \equiv \mathscr{H}(\mathbf{r}, t)$